Investigation of Position Sensitive Avalanche Photodiodes for a New High-Resolution PET Detector Design

Craig S. Levin, *Member, IEEE*, Angela M. K. Foudray, *Student Member, IEEE*, Peter D. Olcott, and Frezghi Habte, *Member, IEEE*

***Abstract*—We are developing a high-resolution PET detector design with a goal of nearly complete scintillation light collection in $\leq$ 1 mm width, $\geq$ 20 mm effective thickness LSO crystals. The design uses position sensitive avalanche photodiodes in novel layered configurations that significantly improve the light collection aspect ratio. To reduce design complexity and dead area we are investigating the use of 1 mm thick sheets of LSO in addition to discrete crystal rods, and the use of PSAPDs which require only four readout channels per device. The raw spatial response of a 1 mm thick crystal sheet coupled to a PSAPD exhibits a compressed dynamic range compared to that observed with discrete crystals. Measurements with the proposed configurations using ^{22}Na irradiation achieved 10%–13% FWHM energy resolution at 511 keV and 2 ns coincidence time resolution. 1 mm width crystals with a saw cut surface finish an no inter-crystal reflector were well resolved in flood images.**

***Index Terms*—Avalanche photodiodes, photodetectors, positron emission tomography (PET), scintillation detectors.**

I. Introduction

RECENTLY, there have been several groups developing high-resolution positron emission tomography (PET) systems dedicated to specific applications such as small laboratory animal and breast cancer imaging [1]–[10]. The standard approach to building high-resolution PET detectors uses an array of minute crystal rods with their narrow ends coupled to a photodetector array. Extracting a significant fraction of the available light from the crystals in this manner proves to be difficult for $\leq$ 1 mm width crystal rods, especially since the rods should also be $>$ 10 mm long for adequate coincident photon detection efficiency. Furthermore, cutting, finishing, and assembling minute crystal arrays is complex and costly.

We are developing a different high-resolution PET detector design that promotes nearly complete scintillation light collection in $\leq$ 1 mm wide, $\geq$ 20 mm effective thickness lutetium oxyorthosilicate (LSO) crystals [11], [12]. We are investigating novel layered configurations of avalanche photodiodes (APDs) that significantly improve the light collection aspect ratio compared to conventional designs (*aspect ratio* is the ratio of crystal readout area to length; a higher ratio improves light collection efficiency).

We have previously studied linear APD arrays coupled to 1 mm thick LSO crystal sheets [12]. A drawback of APD arrays for a PET system is that the readout can be quite complex since each pixel requires its own low noise preamplifier and there are many pixels [12]. To reduce complexity for our high light collection concepts, this paper studies the use of position sensitive APDs (PSAPDs), which require only four readout channels per unit.Thin crystal sheets compared to minute discrete crystals have the advantage that they are less complex to work with and have higher active crystal area, but the disadvantage that the light created from each scintillation event diffuses throughout the crystal. For discrete crystal array approaches we are investigating the conditions of no inter-crystal reflector and saw cut surface finish, which if successful, will greatly reduce crystal array manufacturing complexity.

II. Materials and Methods

A. Scintillation Crystal Configurations

Fig. 1 depicts the high light collection configurations we are investigating in this work, which comprise stacks of scintillation detector layers either edge-on or face-on with respect to incoming 511 keV photons. For high inter-*crystal* packing fraction, the two edge-on concepts shown in Fig. 1 require very thin ($< 300\ \mu$m) PSAPDs that are currently under production. Although the two face-on designs do not require thin PSAPDs, for highest inter-*module* packing fraction they require PSAPDs with minimal surrounding dead area. The scintillation crystal material we have studied was LSO. 1 mm thick sheets of LSO have a very narrow light spread function which minimizes positioning nonlinearities [11], [12].

Since each detector layer in each of these configurations is independent of the others, in this paper we study just one layer to represent the performance of any given configuration. Positioning response of one detector array layer was measured using irradiation with a point ^{22}Na (511 keV) photon source. The crystal sheet layer we studied had dimensions of $8 \times 8 \times 1$ or $8 \times 8 \times 2$ mm^3 and was polished on all sides. The discrete crystal layers we studied were either 4×3 arrays of $2 \times 2 \times 3$ mm^3 or 7×3 arrays of $1 \times 1 \times 3$ mm^3 crystals that each had a ground "as cut"

Manuscript received November 15, 2003; revised February 23, 2004. This work was supported by the National Institutes of Health under Grant EB 003283-01 from the National Institute of Biomedical Imaging and Bioengineering (NIBIB), Grant CA98691-01 from the National Cancer Institute (NCI), and Grant IMG00-000346 from the Susan G. Komen Breast Cancer Research Foundation.

C. S. Levin, P. D. Olcott, and F. Habte are with the Department of Radiology, Stanford University School of Medicine, Stanford, CA 94305-5344 USA (e-mail: cslevin@stanford.edu; pdo@stanford.edu; fhabte@stanford.edu).

A. M. Foudray is with the Physics Department, University of California, San Diego, CA 92037 USA, and also with the Stanford University Medical School, Department of Radiology, Stanford, CA 94305-5344 USA (e-mail: aklohs@physics.ucsd.edu).

Digital Object Identifier 10.1109/TNS.2004.830112

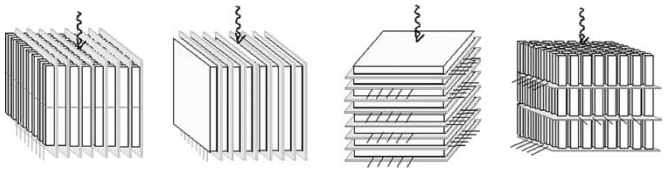

Fig. 1. Four scintillation detector configurations with very high light collection aspect ratio, each comprising layers of scintillation crystals coupled to position-sensing avalanche photodiodes (PSAPDs) (depicted as faint structures with electrical leads in between crystal planes). Within any design the scintillation detector layers are each independent and comprise from left to right: Discrete crystal arrays or crystal sheets oriented "edge-on" with respect to incoming 511 keV photons; Stacked crystal sheets or short stacks of discrete crystal arrays oriented "face-on" with respect to incoming photons. All configurations shown can determine the interaction depth of the 511 keV photons which are shown entering from the top of each detector array.

surface and *no inter-crystal reflector*. The outer faces of the LSO layer (sheet or discrete array) including sides were wrapped in five layers of Teflon tape.

B. Position Sensitive Avalanche Photodiode (PSAPD) Configurations

We used the high gain PSAPDs developed at Radiation Monitoring Devices (RMD), Inc. (Watertown, MA). The devices were fabricated using a planar process similar to that used for APD array fabrication [13]. The prototype PSAPD devices have a sensitive area of 8×8 and 14×14 mm^2. Packaged on a ceramic substrate they are ~ 2 mm thick. In these devices four corner contacts are placed on the backside which is covered by a high resistivity layer. The position of a light flash on the PSAPD front side is positioned using the four corner signals in an Anger-type logic. The energy and timing of each signal may be extracted from the common front surface contact or by summing the four back surface signals.

The operating gain of these devices is approximately 1000 at an operating bias of -1.766 kV on the front surface contact, with the readout anodes at virtual ground. This operating bias provides the best 511 keV photopeak energy resolution in both devices. The PSAPD device capacitances are $\sim$ 45 and 140 pf (0.7 $\mathrm{pf/mm}^2$), the leakage current at operating bias is $\sim$ 300-600 nA and 1–2 $\mu\mathrm{A}$, and the rms noise is $\sim$ 40 and 140 electrons, respectively, for the 8×8 and 14×14 mm^2 devices. The quantum efficiency of these devices are $\geq 60\%$ for the 420 nm peak emission wavelength of LSO.

C. Measurements

We studied spatial and energy response of $^{22}\mathrm{Na}$ 511 keV photon interactions in the LSO scintillation detector layers using both edge-on and face-on irradiation (see Fig. 1). The four back side and common front side APD signals involved in each scintillation event are read out by discrete charge sensitive preamplifiers and NIM electronics, digitized, and sent to a Power Macintosh in list mode for post-processing. Each event was positioned with Anger-type logic. The coincidence time measurements were performed in a standard manner using a PMT coupled to a $6 \times 6 \times 8$ mm^3 LSO crystal to provide the start signal for a time-to-amplitude converter (TAC) with the TAC stop determined from a $8 \times 8 \times 2$ mm^3 LSO sheet coupled to the 8×8 or 14×14 mm^2 PSAPD.

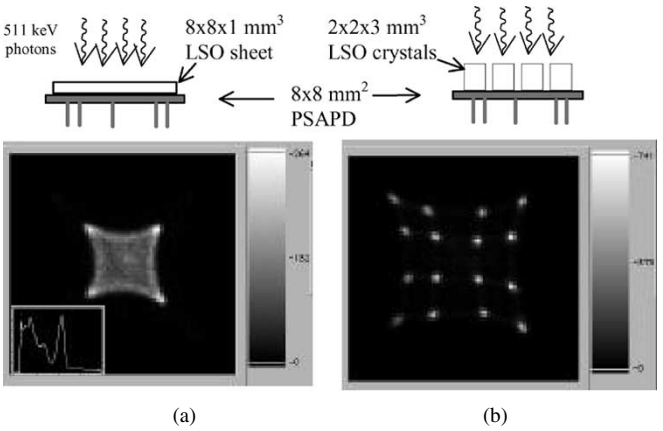

Fig. 2. Two-dimensional histograms of positioned LSO scintillation detector events for one layer from each of the two face-on configurations depicted at the top, using an $8 \times 8\,\mathrm{mm}^2$ PSAPD. (a) Flood image for 1 mm thick crystal sheet. Inset: $^{22}\mathrm{Na}$ energy spectrum with 12.3% FWHM energy resolution for the 511 keV photopeak. (b) Flood image for 4×4 array of $2 \times 2 \times 3\,\mathrm{mm}^3$ crystals.

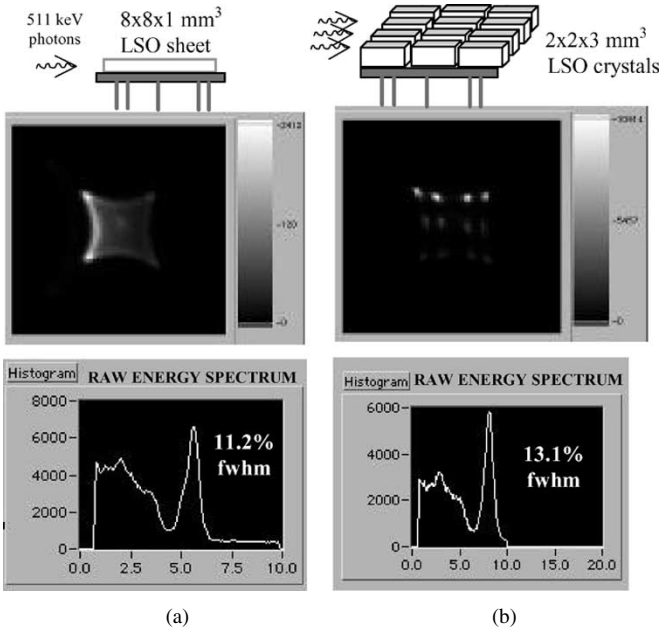

Fig. 3. Two-dimensional histograms of positioned LSO scintillation detector events for one layer from each of the two edge-on irradiated configurations depicted at the top, using an $8 \times 8\,\mathrm{mm}^2$ PSAPD. (a) Image for 1 mm thick crystal sheet. (b) Image for 4×3 array of $2 \times 2 \times 3\,\mathrm{mm}^3$ crystals coupled side-on to the PSAPD; this configuration facilitates a 3 mm interaction depth resolution. Below: Raw $^{22}\mathrm{Na}$ sum energy spectra measured for these two cases.

III. Results

A. Positioning Histograms for the Different Configurations

Fig. 2 shows the 2-D positioning histogram from 511 keV flood irradiation of single scintillation detector layers from the two face-on designs of Fig. 1 comprising either a single crystal sheet or short discrete crystal array coupled to a PSAPD. The $8 \times 8\,\mathrm{mm}^2$ PSAPD was used for these measurements. Note that due to light diffusion and reflections within the crystal sheet, the left flood image in Fig. 2 exhibits a reduced dynamic range compared to that for the discrete crystal array shown at the right. The measured energy spectrum for the sheet is inset.

Fig. 3 shows the measured 2-D histograms and raw sum energy spectra for 511 keV interactions in both the crystal sheet and a

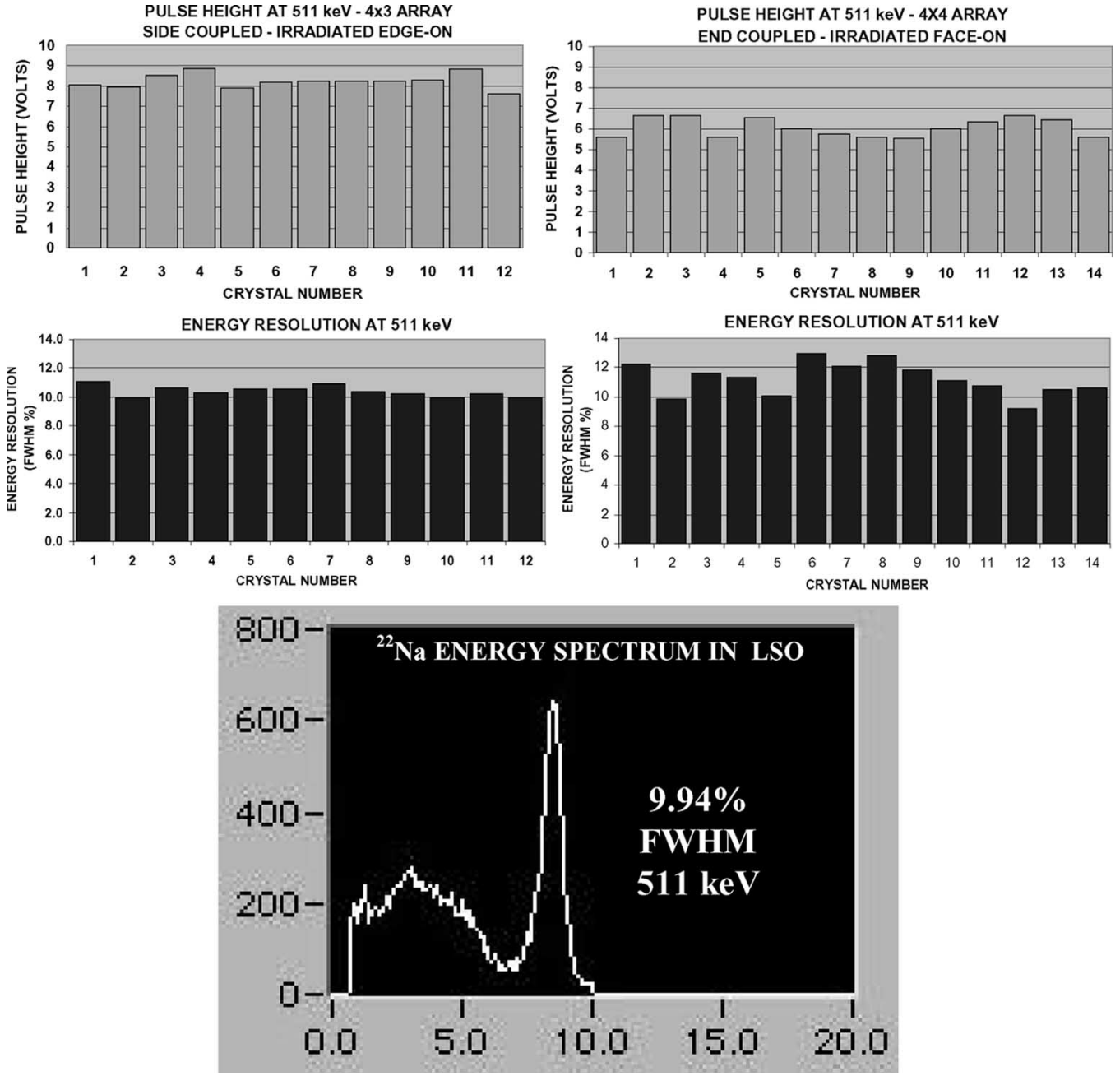

Fig. 4. Comparison between 511 keV photopeak pulse height (top plots) and energy resolution (middle plots) for individual $2 \times 2 \times 3\ \mathrm{mm}^3$ LSO array crystals coupled sideways (left) and end-on (right) to an $8 \times 8\ \mathrm{mm}^2$ PSAPD. Bottom: Best single crystal energy spectrum for the side-coupled array.

discrete crystal array layer relevant to the edge-on irradiation concepts of Fig. 1. For the discrete array, the raw sum energy spectrum incorporates LSO crystal and PSAPD quantum efficiency variations across the detector layer into one spectrum. Thus, for discrete crystal arrays the most accurate technique to extract energy spectra and build calibration tables is through position-gating of individual crystals from the 2-D positioning histograms. As indicated in the top right of Fig. 3, this configuration facilitates a 3 mm interaction depth resolution.

B. Discrete Crystal Position-Gated Energy Spectra Comparisons for Side- and End-Coupled Array Crystals

Fig. 4 shows a comparison of crystal position-gated 511 keV photopeak pulse height and energy resolution extracted from the 2-D positioning histograms for the 4×3 array of $2 \times 2 \times 3\ \mathrm{mm}^3$ LSO crystals coupled sideways to and the 4×4 array of the same crystals coupled end-on to the $8 \times 8\ \mathrm{mm}^2$ PSAPD. We see that even though the $2 \times 2 \times 3\ \mathrm{mm}^3$ crystals are very short, since the light collection aspect ratio is considerably higher for the side-coupled case (3:1) compared to the end-coupled case (4:3) the individual crystal light pulse heights are larger and the variations in pulse height and energy resolution are smaller. The former case had an energy resolution range from 9.9%–11.0% FWHM (average: 10.4%) over the 12 side-coupled array crystals, while that for the latter was 9.9%–13% FWHM (average: 11.2%) for the 16 end-coupled crystals. Also shown is the position-gated energy spectrum with the best photopeak resolution (9.94% FWHM).

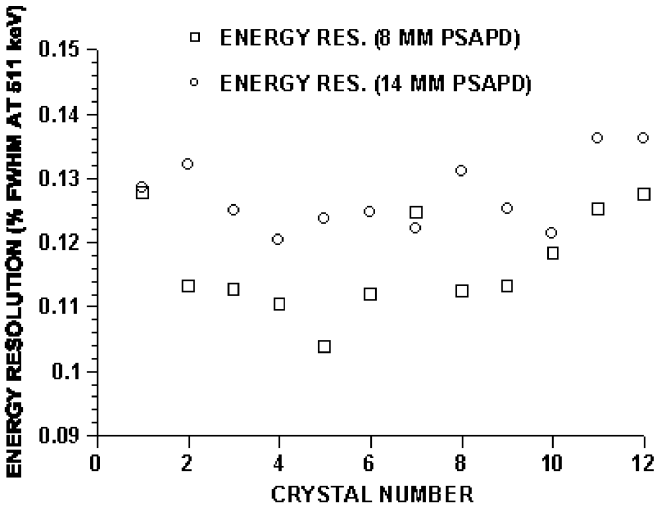

Fig. 5. Plot of 511 keV photopeak energy resolution for individual crystals of a 4×3 array of $2 \times 2 \times 3\ \mathrm{mm}^3$ LSO crystals side-coupled to 8×8 and 14×14 mm^2 PSAPDs (similar to that depicted in Fig. 3, top right).

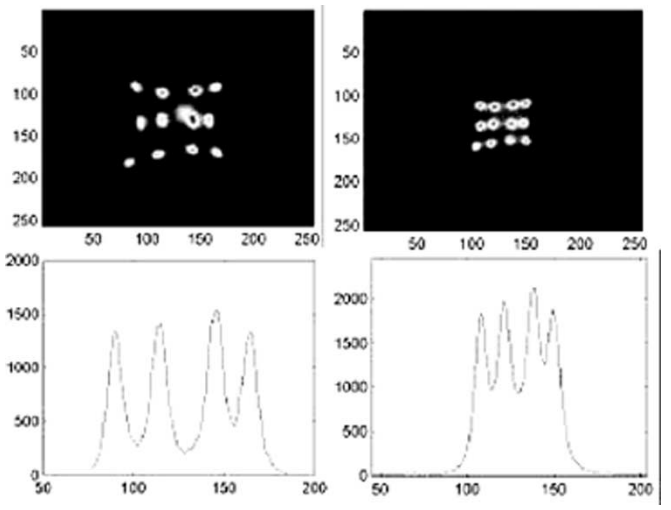

Fig. 6. Top: 2-D $^{22}\mathrm{Na}$ flood histograms of the 4×3 array of $2 \times 2 \times 3\ \mathrm{mm}^3$ LSO crystals side-coupled to the 8×8 (left) and $14 \times 14\ \mathrm{mm}^2$ (right) PSAPDs (similar to that depicted in Fig. 3, top right). Bottom: 1-D profile through top crystal rows of each flood image.

C. Energy Resolution Comparison Between 8×8 and 14×14 mm^2 PSAPD Devices

Fig. 5 shows a comparison between measured photopeak energy resolutions for the individual crystals of the 4×3 array of $2 \times 2 \times 3\ \mathrm{mm}^2$ LSO crystals side-coupled to the 8×8 or $14 \times 14\ \mathrm{mm}^2$ PSAPD. Because the larger area device has higher bulk leakage current and capacitance, the device dark noise and crystal energy resolutions are systematically worse.

D. Discrete Crystal Identification Comparison for 8×8 and 14×14 mm^2 PSAPD Devices

Fig. 6 shows $^{22}\mathrm{Na}$ flood irradiation positioning histograms for the 4×3 array of $2 \times 2 \times 3\ \mathrm{mm}^3$ LSO crystals coupled sideways to the 8×8 and $14 \times 14\ \mathrm{mm}^2$ PSAPDs. Also shown is the 1-D profile histogram through one of the crystal rows. Because the larger area device has higher bulk leakage current and capacitance, the crystal peak to valley ratios are systematically worse and the crystals are not as clearly distinguished.

E. Coincidence Time Resolution Measurements With the 8×8 and 14×14 mm^2 PSAPD Devices

Fig. 7 shows the measured TAC spectra for coincidences between the LSO-PMT and LSO-PSAPD channels. "Raw" TAC spectra data used a threshold just above the noise level in both the PMT and PSAPD. "Energy gated" TAC data used a 20% window about the 511 keV photopeak in each channel. The coincidence time resolution directly depends upon the fluctuation in the slope of the pulse rise in each channel. Since the $14 \times 14\ \mathrm{mm}^2$ PSAPD dark noise is worse and the capacitance is higher, the pulse rise variations are higher and the TAC spectra are broader (~ 3.3-3.4 ± 0.1 ns FWHM) compared to that for the $8 \times 8\ \mathrm{mm}^2$ device (~ 2.0-2.8 ± 0.1 ns).

F. PSAPD Readout of 1 mm Crystal Array

Fig. 8 shows results for an 7×3 array of $1 \times 1 \times 3\ \mathrm{mm}^3$ LSO crystals side-coupled to the $8 \times 8\ \mathrm{mm}^2$ PSAPD, flood irradiated with a $^{22}\mathrm{Na}$ source. In this measurement the top nine crystals appearing in the flood image were saw cut on all faces, while the bottom 12 crystals were polished. The crystals were placed in the array without intercrystal reflector. The 1 mm array crystals were easily identified with peak/valley ratios ranging from 2 to 9. Three of the crystals were slightly off the edge of the sensitive area and recorded photopeak energy resolutions greater than 13.9% FWHM. The remaining crystals had 511 keV photopeak energy resolutions of less than 13% FWHM. The best $1 \times 1 \times 3\ \mathrm{mm}^3$ individual LSO crystal 511 keV photopeak energy resolution was 9.7% FWHM with saw-cut (coarse ground) surfaces and no inter-crystal reflector (see bottom right of Fig. 8).

IV. Summary and Discussion

Our goal is to develop an ultra-high-resolution detector with high detection efficiency, photon interaction depth resolution, and nearly complete collection of the available scintillation light from a 511 keV photon interaction. Optimizing light collection is important for robust light signals and high energy resolution. Excellent energy resolution allows one to use a narrow energy window about the photopeak, while still maintaining high count sensitivity. A narrow pulse height window reduces random and scatter background contamination and in doing so also helps to improve count rate performance.

The first three proposed configurations (Fig. 1) utilize layers of large area, position sensitive avalanche photodiodes that readout large faces of scintillation crystals for very high light collection aspect ratios. For these three configurations nearly all available light is collected, independent of the crystal geometry and surface finish. This property can be seen from the very similar energy resolutions measured from $2 \times 2 \times 3$ and $1 \times 1 \times 3\ \mathrm{mm}^3$ LSO crystals, for saw cut or polished surfaces (see Figs. 4 and 8). 1 mm discrete crystals are well resolved even with no inter-crystal reflector and especially with saw cut finish Fig. 8. The fourth configuration in Fig. 1 utilizes short stacks of discrete crystals coupled end-on to the PSAPD. The light collection aspect ratio in this case is not as

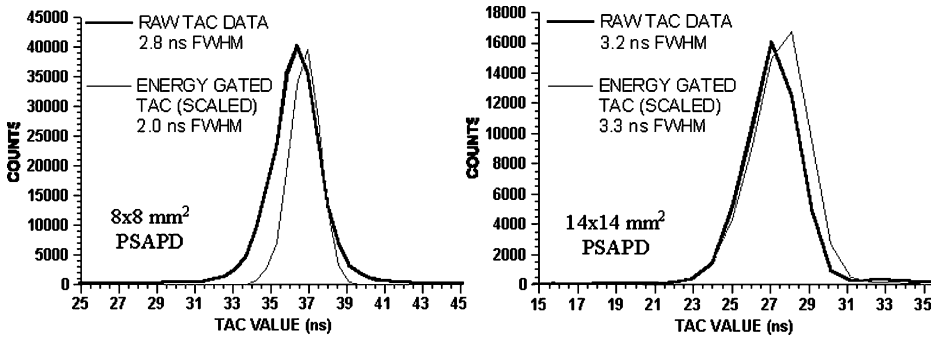

(a) (b)

Fig. 7. Coincidence TAC spectra measured with (a) the 8×8 and (b) $14 \times 14\ \mathrm{mm}^2$ PSAPDs. The fitting errors in the quoted resolutions are $\pm 0.1\ \mathrm{ns}$.

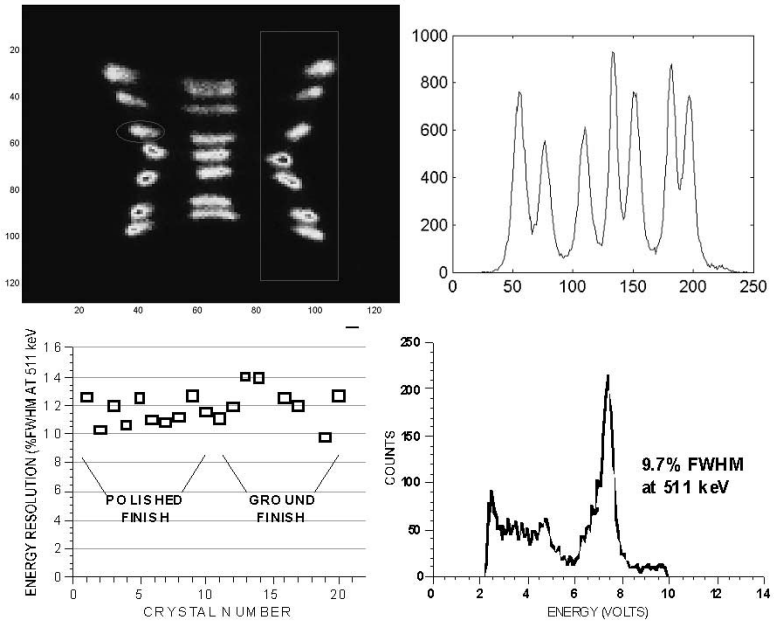

Fig. 8. Top left: 2-D $^{22}\mathrm{Na}$ flood histogram of 7×3 array of $1 \times 1 \times 3\ \mathrm{mm}^3$ LSO crystals side-coupled to the $8 \times 8\ \mathrm{mm}^2$ PSAPD (in a manner similar to that depicted in Fig. 3, top right). The surfaces of the top nine crystals were saw cut, while those of the bottom 12 crystals were polished. No intercrystal reflector was used. Top right: Profile through one column of crystal array flood image indicates the excellent peak separation achieved for either surface condition. Bottom left: Plot of photopeak energy resolutions for 10 of 12 polished and 8 of 9 saw-cut array crystals. Bottom right: The best crystal energy spectra came from a saw-cut crystal indicated by a small ellipse in the flood image.

high as for the other three configurations and, as a result, the pulse heights are smaller and both pulse height and energy resolution variations among crystals are larger compared to the side-coupled case (see Fig. 4). Thus, we will no longer pursue the end-coupled design. Edge-on orientations require very thin ($< 300\ \mathrm{microns\ thick}$) APDs, which are currently being developed.

Use of crystal sheets instead of arrays of minute discrete crystals is desirable to reduce detector manufacturing complexity. Also, the positioning is continuous and the resolution binning selectable in both directions. However, due to light diffusion throughout the sheet crystal for every event, using Anger-type logic on the four corner signals for event positioning yields a compressed spatial dynamic range compared to the discrete crystal case (Fig. 2) since the maximum difference between signals along any given direction is reduced. Spatial compression also occurs for the side-coupled discrete crystal arrays (Figs. 3, 6 and 8) since there were no reflectors between crystals used in these studies and intercrystal light sharing occurred (although not as much for the $1 \times 1 \times 3\ \mathrm{mm}^3$ crystal array, see Fig. 8). More intelligent positioning algorithms [14] are under investigation to expand the dynamic range of the sheet crystal positioning and improve linearity near the FOV edge. Note the measured dynamic range also improves by 28% if we remove the crystal edge reflector, but this reduces the measured light collection by 27% and energy resolution by 16%.

The 8×8 and $14 \times 14\ \mathrm{mm}^2$ PSAPDs were compared with regard to 511 keV photopeak energy resolution, discrete crystal identification and coincidence time resolution for the same LSO crystals. In all cases the $8 \times 8\ \mathrm{mm}^2$ array performed systematically better than the larger PSAPD. The energy resolution ranged from $\sim$ 10-13% FWHM in the former while that for the latter was $\sim$ 12-14%. The crystal peak to valley ratios in the 2-D discrete crystal $2 \times 2 \times 3\ \mathrm{mm}^3$ positioning histograms ranged from $\sim$ 3-6 for the $8 \times 8\ \mathrm{mm}^2$ device, but only $\sim$ 1.3-2 for the larger device. Finally, the coincidence time resolution measured using a 20% window about the photopeak in each channel was 2.0 ns FWHM in the $8 \times 8\ \mathrm{mm}^2$ device compared to 3.3 ns in the

larger device. However, the $14 \times 14\ \mathrm{mm}^2$ device offers the distinct advantage of a factor of three larger sensitive area, which means a factor of three fewer devices and electronic channels are required for the same system scintillation crystal volume.

Achieving $> 20\ \mathrm{mm}$ effective LSO thickness for the edge-on configurations (Fig. 1, left two designs) would require detector arrays stacked two and three modules deep, respectively, using the 14×14 and $8 \times 8\ \mathrm{mm}^2$ PSAPDs. The number of devices require to achieve the desired LSO depth for the third (face-on) design in Fig. 1 depends upon the crystal thickness utilized.

V. Conclusion and Future Directions

Our results indicate that PSAPDs can be used for high light collection configurations to optimize PET detector performance parameters such as energy, spatial and temporal resolutions. Presently we are taking steps to realize the detector modules depicted in Fig. 1. For the first two edge-on designs we are currently developing a $< 300\ \mu\mathrm{m}$ thick PSAPD which will facilitate a 70% crystal packing fraction. Our experiments indicate that arrays of discrete saw cut crystals with no intercrystal reflector can be used, which reduces detector complexity and improves crystal packing fraction. For the sheet crystal designs we are investigating intelligent algorithms to improve the spatial dynamic range and linearity. To take full advantage of the high gain provided by the PSAPD we are developing compact, high input dynamic range, leakage current compensated front-end readout electronics.

Acknowledgment

The authors would like to acknowledge D. Farrel, M. McClish, M. Squillante, and K. Shah at RMD, Inc. for their ideas and support.

References

[1] R. S. Miyaoka, S. G. Kohlmyer, and T. K. Lewellen, "Performance characteristics of micro crystal element (MiCE) detectors," *IEEE Trans. Nucl. Sci.*, pt. 2, vol. 48, pp. 1403–1407, Aug. 2001.

[2] Y.-C. Tai, A. F. Chatziioannou, and S. Siegel *et al.*, "Performance evaluation of the microPET P4: A PET system dedicated to animal imaging," *Phys. Med. Biol.*, vol. 46, no. 7, pp. 1845–1862, July 2001.

[3] C. J. Marriott *et al.*, "High resolution PET imaging and quantitation of pharmaceutical biodistributions in a small animal using APD detectors," *J. Nucl. Med.*, vol. 35, pp. 1390–1397, 1994.

[4] C. Schmelz *et al.*, "Feasibility study of an avalanche photodiode readout for a high-resolution PET with nsec time resolution," *IEEE Trans. Nucl. Sci.*, vol. 42, pp. 1080–1084, 1995.

[5] A. F. Chatziioannou *et al.*, "Performance evaluation of microPET: A high-resolution lutetium oxyorthosilicate PET scanner for animal imaging," *J. Nucl. Med.*, vol. 40, pp. 1164–1175, 1999.

[6] A. P. Jeavons, R. A. Chandler, and C. A. Dettmar, "A 3-D HIDAC-PET camera with sub-millimeter resolution for imaging small animals," *IEEE Trans. Nucl. Sci.*, pt. 2, vol. 46, pp. 468–73, June 1999.

[7] V. G. Zavarzin, H. A. Kudrolli, P. Y. Stepanov, I. N. Weinberg, L. P. Adler, and W. A. Worstell, "First results with PEM-X, a compact modular PET breast imager" (in Abstract M3-37), in *Proc. IEEE Medical Imaging Conf.*, Seattle, WA, Oct. 26–30, 1999.

[8] N. Zhang, C. J. Thompson, D. Togane, F. Cayouette, and K. Q. Nguyen, "Anode position and last dynode timing circuits for dual-layer BGO scintillator with PS-PMT based modular PET detectors," *IEEE Trans. Nucl. Sci.*, pt. 1, vol. 49, pp. 2203–2207, Oct. 2002.

[9] M. F. Smith, S. Majewski, A. G. Weisenberger, D. A. Kieper, R. R. Raylman, and T. G. Turkington, "Analysis of factors affecting positron emission mammography (PEM) image formation," *IEEE Trans. Nucl. Sci.*, vol. 50, pp. 53–59, Feb. 2003.

[10] R. Freifelder, C. Cardi, I. Grigoras, J. R. Saffer, and J. S. Karp, "First results of a dedicated breast PET imager, BPET, using NaI(Tl) curve plate detectors," in *Proc. 2001 IEEE Nuclear Science Symp. Conf Rec.*, vol. 3, San Diego, CA, Nov. 4–10, 2001, pp. 1241–1245.

[11] C. S. Levin, "Design of a high-resolution and high-sensitivity scintillation crystal array for PET with nearly complete light collection," *IEEE Trans. Nucl. Sci.*, vol. 49, pp. 2236–2243, Oct. 2002.

[12] C. S. Levin and F. Habte, "Initial sudies of a new detector design for ultra-high-resolution positron emission tomography," in *Proc. 2002 IEEE Nuclear Science Symp. Conf. Rec.*, Norfolk, VA, Nov. 10–16, 2002, IEEE Nucl. Sci., vol. 3, pp. 1751–1755, 2003.

[13] K. S. Shah, R. Farrell, R. Grazioso, R. Myers, and L. Cirignano, "Large-area APDs and monolithic APD arrays," *IEEE Trans. Nucl. Sci.*, pt. 2, vol. 48, pp. 2352–2356, Dec. 2001.

[14] J. Joung, R. S. Miyaoka, and T. K. Lewellen, "cMiCE:A high-resolution animal PET using continuous LSO with a statistics based positioning scheme," in *Proc. 2001 IEEE Nuclear Science Symp. Conf. Rec.*, vol. 2, San Diego, CA, Nov. 4–10, 2001, pp. 1137–1141.